Numerical Analysis of the Vapor Flow in an Axially Rotating Heat Pipe in Drilling Processes

GUSTAVO GUTIERREZ[1] AND TIEN-CHIEN JEN[2*]

[1] *Mechanical Engineering Department, University of Puerto Rico
Mayaguez, Puerto Rico 00681-9045*
[2] *Mechanical Engineering Department, University of Wisconsin,
Milwaukee, WI 53211, USA*

Heat pipes offer an effective alternate to conventional methods of removing heat from a drill tip, allowing drilling operations in a dry and environmentally friendly fashion. In this study, a model of the vapor flow in an axially rotating heat pipe is developed. A control volume numerical approach and a staggered grid are used in the development of the computer program. Suction and blowing velocities at the inner wall of the heat pipe are related to a local heat flux input in the evaporator section, and local heat output in the condenser section, respectively. A parametric study is conducted for different rotating speeds and different saturation temperatures of the working liquid of the heat pipe. These parameters significantly affect the hydrodynamics of the vapor flow. It is observed that the vapor flow is strongly influenced by increasing rotating speeds, eventually resulting in flow reversal. It is also found that the saturation temperature has a strong effect on vapor flow velocity distributions. The result of this study will be helpful for further and more complete analysis including the effects of the flow in the liquid film and heat transfer performance of the rotating heat pipe drill.

Keywords: Vapor flow, Heat pipes, Axially rotating heat pipes

INTRODUCTION

In any machining process, most of the input energy is converted into heat at the cutting zone. This results in an increase in tool and workpiece temperatures. Elevated temperature can significantly shorten the tool life. Excessive heat accumulated in the tool and workpiece can contribute to thermal distortion and poor dimensional control of the workpiece. In addition, high tool temperatures promote the formation of BUE (build-up edge) on the tool tip.

In drilling, tool temperatures are particularly important because the chip, which absorbs much of the cutting energy, is generated in a confined space and remain in contact with the tool for a relatively long time compared with other machining operations. As a result, drill temperatures are much higher than in other processes under similar conditions. The most

* Corresponding Author: E-mail: jen@cae.uwm.edu, Tel: (414)-229-2307, Fax: (414) 229-6958

common cooling method is the use of cutting fluids to flood the cutting zone. However, disposal of the used fluids is subject to federal, state and local laws and regulations (Kalpakjian, 1995). It has been documented that the cost of compliance with regulations and the annual operation cost in the maintenance and disposal of these cutting fluids in a typical production plant can represent an important part of the total operating cost. For example, the estimated cost attributed to coolant usage is between 7-16% of the total operating cost in the U.S. and up to 25% in Germany. More stringent environmental regulations are expected in the future and we can expect the cost associated with coolants to continue to rise (DeVries and Murray, 1994 and Labattaille and Manjunathaiah, 1999).

As a result of the costs associated with use of cutting fluids, recently, there has been a strong global trend towards the minimization of cutting fluids. The NSF Environmentally Conscious Manufacturing initiative guidelines have put a major emphasis on research topics that address the elimination of metalworking fluids. In order for machining process to run dry, an effective cooling method, other than flooding by a coolant, needs to be developed to remove the heat accumulated in the drilling tool.

Heat pipes offer an effective alternate to removing heat without significant increases in operating temperatures. A heat pipe is a passive device that transports energy with relatively low temperature difference without the need for an external power supply. The components of a heat pipe are a sealed container (pipe wall and end caps), and a small amount of working fluid in equilibrium with its own vapor. Typically, a heat pipe can be divided into three sections: the evaporator section, the adiabatic (transport) section and the condenser section (see Figure 2). The external heat load on the evaporator section causes the working fluid to vaporize. The resulting vapor pressure drives the vapor through the adiabatic section to the condenser section, where the vapor condenses, releasing its latent heat of vaporization to the provided low temperature environment. The condensed working fluid is then pumped back either by capillary pressure generated by the meniscus in the wick structure or by centrifugal effects in rotating pipes. Transport of heat can be continuous as long as there is sufficient driving forces generated to return the condensed liquid back to the evaporator. A detailed literature review on the-state-of-art development in heat pipes can be found in Faghri (1995) and Peterson (1994).

Even though the application of heat pipes in cooling a drill tool has been mentioned in the literature, to the best knowledge of the authors, there has been no actual study of this application. Most previous investigations in rotating heat pipes have used a Nusselt-type analysis for the liquid film (wickless heat pipes) (Ballback, 1969; Chan, *et al.* 1971; Daley, 1970; Daniels and Al-Jumaily, 1975; Gray, 1969; Harley and Faghri, 1995). Lock (1992) presented a comprehensive study on the thermosyphon including stationary and rotating thermosyphons. Peterson and Wu (1991) gave a detailed review of rotating and revolving heat pipes. These authors indicate that the performance of rotating heat pipes without an internal taper is mainly affected by rotating speed, working fluid fill ratio, properties of the working fluid, working temperature, inclination angle and wick structure. In rotating heat pipes with an internal taper, they found that the rotational speed is the most significant parameter. Daniels and Al-Jumaily (1975) carried out an investigation of the factors affecting the performance of a rotating heat pipe. The authors performed a theoretical analysis of the condensation process using a Nusselt-type approach. Their analytical results were validated with experimental data for rotating speed between 600 and 1200 rpm. They concluded that the rotating effect enhances the heat transfer capability, but the rate of increase of heat transfer tends to decline indicating an upper rotating speed limit. For drilling applications, an internal heat pipe has some manufacturing constraints. For example, the heat pipe location cannot get too close to the drilling tip, and the contact resistance between the heat pipe and the drill tool can significantly affect the performance of the heat pipe. Detailed preliminary analyses on these constraints, with experimental verification, can be found in Jen, *et al*. (2002).
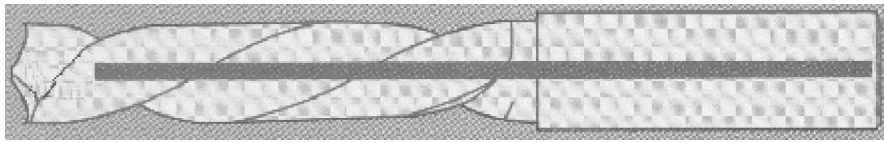
FIGURE 1
Location of heat pipe inside drill.

In this study, a numerical model of the vapor flow in an axially rotating heat pipe is developed. Suction and blowing velocities at the inner wall of the heat pipe were assumed. Note that in actual drilling operations, the suction and blowing velocities at the inner wall of the heat pipe are related to a local heat flux input in the evaporator section, and local heat output in the condenser section, respectively. A parametric study is conducted for different rotating speeds and different saturation temperatures of the working liquid of the heat pipe. These parameters significantly affect the hydrodynamics of the vapor flow. It is observed that the vapor flow becomes strongly asymmetric when rotating speed is increased, with the eventual appearance of flow reversal. The result of this study will be beneficial for further and more complete analysis on the interaction between the vapor flow and the liquid flow. The vapor flows in a heat pipe is in opposite direction to the liquid flow. At high vapor velocity, the shear stress at the vapor-liquid interface could be sufficient to disrupt the liquid flow, producing an entrainment limit of the heat pipe. The shear stress at the interface is proportional to the velocity gradient of the vapor. These parameters are a very strong function of the saturation temperature of the vapor and the rotating speed of the pipe. In this study, the hydrodynamics of the vapor flow is investigated in detail for different saturation conditions. It is worth noting that this effect has been overlooked from the literature (e.g., Faghri, *et al.*, 1993 and Harley and Faghri, 1995).

THE PHYSICAL MODEL

The idea of using a heat pipe in a drilling tool is illustrated in Figure 1. In drilling operations, most of the heat is generated near the drilling tip. This heat accumulated near the drilling tip can cause various thermal damages to the drill as well as the workpiece, such as tool wear, large thermal residual stresses, thermal expansion and the reduction of the geometric accuracy. With heat pipe implemented in the drill, the heat penetrates into the drill can be absorbed quickly by the heat pipe. With latent heat evaporation in the evaporation section (i.e., near the drill tip), this heat can be transported rapidly to the condenser section (drill shank). Note that drill shank is usually attached to the drill holder, which has a large mass and can be viewed as a heat sink. Therefore, the drill tip temperature can be greatly reduced. The latest experimental results show that the temperature reduction in a heat pipe drill compared to a solid drill can reach more than 50% (Gutierrez and Jen, 2002).

Figure 2 shows the physical configuration of a heat pipe. It can be seen from the figure that there is vapor flow flowing from evaporator section toward the condenser section in the core region, with the condensed liquid flowing back to the evaporator section along the pipe inner wall. In this paper, attention is focused on the vapor flow in the core region of the heat pipe. To uncouple the conjugated heat transfer problem with the pipe wall, an assumption is needed about the heat flux input at the evaporator section and the heat flux output at the condenser section, both heat fluxes being related to blowing and suction flow conditions at these sections. It is assumed that a triangular heat flux distribution is present at the evaporator and a uniform heat flux distribution is present at the condenser. This triangular heat flux distribution is a reasonable assumption because higher heat flux is generated at the tip of the drill. Note that, under steady state condition, the
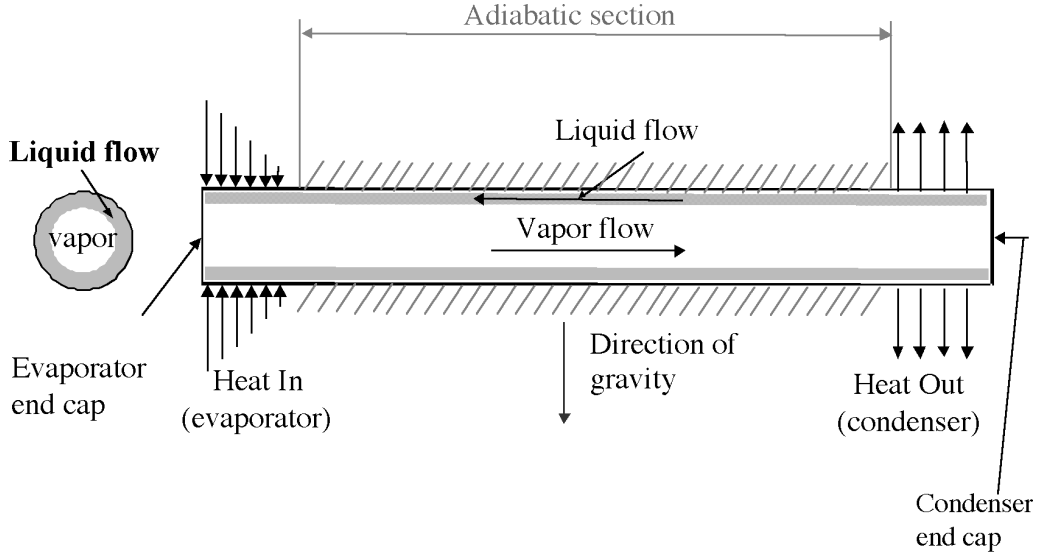
FIGURE 2
Schematic of the Heat Pipe.

amount of heat entering the pipe through evaporator section must be equal to the total heat leaving the condenser section. Thus, the heat flux removed from the condenser section can be easily estimated. In this study, water is selected as the working fluid; vapor is assumed to be a saturated ideal gas and the flow is assumed to be laminar and incompressible.

Mathematical Formulation

Evaporation and condensation are considered uniform around the circumferential direction. Based on this assumption, the problem becomes axis-symmetric and all the derivatives with respect to the circumferential direction are zero. Thus, the problem becomes two-dimensional in cylindrical coordinates. However, in axis-symmetric swirling flow the momentum equation in the circumferential direction has to be solved as well. The conservation equations for the vapor flow with the axis-symmetric condition become:

Conservation of mass

$$\frac{1}{r}\frac{\partial}{\partial r}(rV_r) + \frac{\partial V_z}{\partial z} = 0 \tag{1}$$

Momentum equation in the radial direction

$$\frac{1}{r}\frac{\partial(\rho r V_r V_r)}{\partial r} + \frac{\partial(\rho V_r V_z)}{\partial z} = -\frac{\partial \hat{p}}{\partial r} +$$

$$\mu\left(\frac{1}{r}\frac{\partial}{\partial r}(r\frac{\partial V_r}{\partial r}) + \frac{\partial^2 V_r}{\partial z^2} - \frac{V_r}{r^2}\right) + \frac{\rho V_\theta^2}{r} + 2\rho \Omega V_\theta \tag{2}$$

Momentum equation in the circumferential direction

$$\frac{1}{r}\frac{\partial(\rho r V_\theta V_r)}{\partial r} + \frac{\partial(\rho V_\theta V_z)}{\partial z} =$$

$$\mu\left(\frac{1}{r}\frac{\partial}{\partial r}(r\frac{\partial V_\theta}{\partial r}) + \frac{\partial^2 V_\theta}{\partial z^2} - \frac{V_\theta}{r^2}\right) - \frac{\rho V_r V_\theta}{r} - 2\rho \Omega V_r \tag{3}$$

Momentum equation in the axial direction

$$\frac{1}{r}\frac{\partial(\rho r V_z V_r)}{\partial r} + \frac{\partial(\rho V_z V_z)}{\partial z} =$$

$$-\frac{\partial \hat{p}}{\partial z} + \mu\left(\frac{1}{r}\frac{\partial}{\partial r}(r\frac{\partial V_z}{\partial r}) + \frac{\partial^2 V_z}{\partial z^2}\right) \tag{4}$$

where p is the reduced pressure

$$\hat{p} = p - \frac{1}{2}\rho\,\Omega^2 r^2 \qquad (5)$$

and V_r, V_θ and V_z are the radial, circumferential and axial velocities respectively. Note that the coordinate system is assumed fixed to the rotating pipe (non-inertial frame); then, the Coriolis acceleration appears explicitly in the momentum equations. The centrifugal acceleration is combined with the pressure and it does not appear explicitly (see equation (5))
It is worth noting the momentum equation in the radial and circumferential direction have additional coupling through the terms $\dfrac{\rho V_\theta^2}{r}$ and $2\rho\Omega V_\theta$ in the r direction and $\dfrac{\rho V_r V_\theta}{r}$ and $2\rho\Omega V_r$ in the θ direction. Special treatment of these terms is required, and is discussed in the next section. If the coordinate system is assumed to be an inertial frame (not-fixed to the rotating pipe) the terms $2\rho\Omega V_\theta$ and $2\rho\Omega V_r$ do not appear explicitly in equations (2) and (3) respectively.

Boundary Conditions

At the center line of the pipe (from symmetry)

$$V_r = V_\theta = \frac{\partial V_z}{\partial r} = 0 \qquad (6)$$

Since the coordinate system is fixed to the rotating pipe, at the end caps of the pipe ($z=0$ and $z=L$), the radial and axial velocities are zero (no-slip condition). At the inner wall of the heat pipe ($R_0 = D/2$), the circumferential and radial velocities are assumed zero (no-slip condition, no interfacial stresses are considered). For the inertial frame, the non-slip condition at the walls for the circumferential velocity is $V_\theta = \Omega r$ instead of zero as it is for the non-inertial frame. From the theoretical point of view, the choice of the reference frame is irrelevant but from the numerical point of view, using the rotating frame (i.e., non-inertial frame) results in better numerical stability.

Evaporation and condensation at the inner wall of the evaporation region and the condensation region of the heat pipe are modeled as blowing and suction velocities (Faghri, *et al.*, 1993) and are related to the local heat rate as:

$$V_w = \pm\frac{q(z)}{\pi\,D\,\rho\,h_{fg}} \qquad (7)$$

where $q(z)$ is the local rate of heat transfer per unit length, D is the diameter of the heat pipe, ρ is the density of the vapor and h_{fg} is the latent heat of vaporization. The positive sign corresponds to suction action in the condenser and the negative sign corresponds to the blowing action in the evaporator. The saturation temperature is related to the saturation pressure at the liquid-vapor interface for an ideal gas, through the Clausius-Clapeyron equation:

$$T_{sat} = \left[\frac{1}{T_0} - \frac{R_v}{h_{fg}}\ln\frac{P_{sat}}{P_0}\right]^{-1} \qquad (8)$$

here T_0 and P_0 are reference temperature and pressure at saturation condition (i.e. 1.01×10^5 Pa and 373 K) and R_v is the gas constant for the vapor. The density of the vapor is linked to the saturation temperature and saturation pressure through the equation of state for an ideal gas:

$$P_{sat} = \rho\,R_v\,T_{sat} \qquad (9)$$

At the adiabatic region the radial velocity is assumed to be zero (impermeable wall) as well as the circumferential and axial velocities (no-slip condition). Figure 3 shows the physical domain and the coordinate system of a rotating heat pipe.
The development of the friction coefficient along the pipe in the plane *r-z*, can be defined as:

$$f = \frac{\tau_w}{\frac{1}{2}\rho V_w^2} = \frac{\mu\left.\dfrac{\partial V_z}{\partial n}\right|_w}{\frac{1}{2}\rho V_w^2} = \frac{\left.\dfrac{\partial V_z^*}{\partial n^*}\right|_w}{\mathrm{Re}} \qquad (10)$$
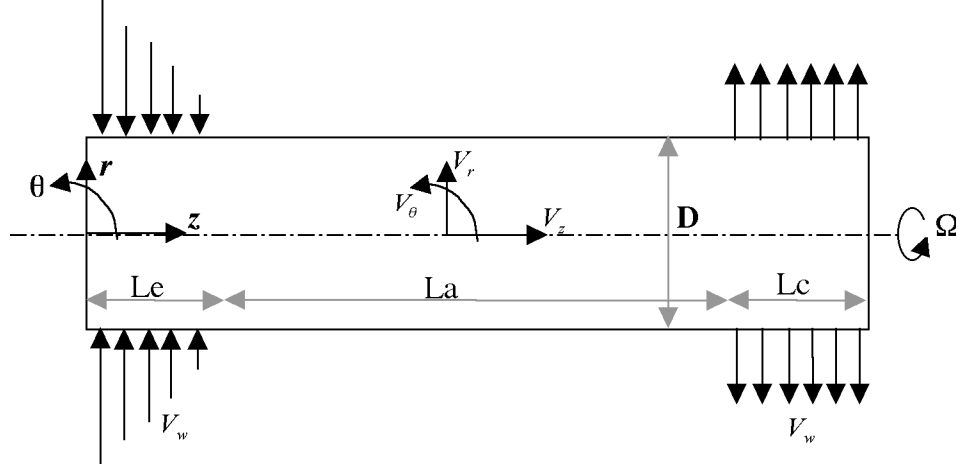
or

FIGURE 3
Physical domain and coordinate.

$$f\,\text{Re} = \left.\frac{\partial V_z^*}{\partial n^*}\right|_w \tag{11}$$

Here, V_Z^* and n^* are the dimensionless axial velocity and the dimensionless direction normal to the wall.

For all the cases presented in this study the Reynolds number is the same, so the friction coefficient f is a measure of the axial velocity gradients at the wall.

Numerical Modeling

For the purposes of the numerical analysis, it is useful to have a generic conservation equation, from which the equations of conservation of mass and momentum are obtained. This generic conservation equation in cylindrical coordinates can be written as:

$$\frac{1}{r}\frac{\partial(\rho\,rV_r\phi)}{\partial r} + \frac{\partial(\rho\,V_z\phi)}{\partial z} = \Gamma\left(\frac{1}{r}\frac{\partial}{\partial r}(r\frac{\partial\phi}{\partial r}) + \frac{\partial^2\phi}{\partial z^2}\right) + S_\phi \tag{12}$$

where ϕ is a generic property, Γ is the diffusivity for the generic property ϕ, and S_ϕ is the source term. It can be seen from Table 1 that one can reproduce the governing equations from this generic equation. The advantage of the generic conservation equation in

development of the numerical code because one needs to deal with only a single equation of that form. Note that, for convenience, the pressure gradient term is included in the source term in equation (12). In the numerical scheme, this term is treated separately since the pressure field has to be obtained as part of the solution. A pressure correction (or pressure equation) is derived from the momentum equation to enforce mass conservation. This is the basis of the SIMPLE-like algorithms (Patankar, 1980).

The discretization in cylindrical coordinates generates additional coupling between the momentum equations as shown in Table 1. These terms are treated as extra body forces including the Coriolis force terms

(i.e., $2\rho\Omega V_\theta$ and $2\rho\Omega V_r$). The terms $\rho\dfrac{V_r V_\theta}{r}$ and $\mu\dfrac{V_\theta}{r^2}$

in the θ-momentum equation are treated implicitly when the contribution of these terms to the central coefficient in the discretized equations are positive, in order to avoid instabilities of the iterative solution scheme that can occur when diagonal dominance of the matrix is not maintained. Otherwise, these terms are treated explicitly. A control volume approach is used to discretize the governing equations. The generic equation is discretized using the power law

TABLE 1
Terms in the Generic Conservation Equation.

ϕ	Γ	S_ϕ	Equation
1	-	0	continuity
V_r	μ	$-\dfrac{\partial p}{\partial r} + \rho \dfrac{V_\theta^2}{r} + 2\rho\Omega V_\theta$	r-momentum
V_θ	μ	$-\rho \dfrac{V_r V_\theta}{r} - \mu \dfrac{V_\theta}{r^2} - 2\rho\Omega V_r$	θ-momentum
V_z	μ	$-\dfrac{\partial p}{\partial z}$	z-momentum

scheme (Patankar, 1980). The pressure velocity coupling is solved using the SIMPLEC algorithm (Van Doormal and Raithby, 1984)

Numerical procedure

1. Solve the V_r, V_θ and V_z momentum equations simultaneously using the current values for pressure and velocities (in the first iteration a zero velocity and pressure field is assumed, except at the boundaries where the boundary conditions are applied).
2. Since the velocities obtained in Step 1 may not satisfy the continuity equation locally, the pressure correction equation is solved to obtain the necessary corrections for the velocity field (using the SIMPLEC algorithm the pressure does not need a correction).
3. Correct the velocity field until continuity is achieved.
4. Repeat Steps 1 to 3 until the residual of the momentum equations and pressure equation are less than a pre-assigned convergence criterion.

The convergence criterion used is the residual of each equation less than 10^{-6}. Grid independence was checked by systematically varying the number of control volumes in the r and z directions until the

solution was adequately grid independent. Table 2 summarizes the grid refinement test. For this test, the case with a rotational speed $\omega =1200$ rpm and operating temperature $T_{sat} = 100$ ºC was selected. The test is performed for three different grid sizes and the maximum dimensionless axial velocities at the middle of the evaporator, adiabatic and condenser section are compared. The maximum change is less than 2.5 % when the grid size change from 100×40 to 150×60. A grid size of 100×40 was selected for all the calculations. The computational domain was divided in three sub-domains: evaporator, adiabatic region, and condenser. A number of 20 control volumes were used for the evaporator and condenser respectively and 60 control volumes for the adiabatic region. In the radial direction 40 control volumes were used.

RESULTS AND DISCUSSION

In the discussion that follows, the axial, radial and circumferential velocity profiles at different rotating speeds and axial locations will be examined closely. The effect of different saturation conditions on the velocity profiles will be demonstrated. Note that this effect has *never* been investigated in any previous studies. A

TABLE 2
Grid Independence Test.

	Section at the middle of:	Grid size		
		80×32	100×40	150×60
Maximum Dimensionless axial velocity	Evaporator	8.86	8.87	8.78
	Adiabatic	10.09	10.08	10.08
	Condenser	8.39	8.56	8.76

benchmark comparison with numerical results presented by Faghri, *et al.* (1993) is also presented.

For comparison purpose, the results from Faghri, *et al.* (1993) are reproduced in Figure 4. The velocity profiles in Figures 4 and 5 are nondimensionalized using the average axial velocity at the adiabatic region, $V_z = 4V_wLc/D$, as the reference velocity. Here, the axial velocity profiles for a uniform heat flux (uniform blowing and suction velocities) for different rotating speeds and a Reynolds number of *Re=0.01* are used. For this test the following parameters are applied: *Le=0.20* m, *La=0.6 m*, *Lc=0.2* m, *D=0.02* m with saturation temperature at 100 °C. The present numerical simulation has successfully reproduced Faghri, *et al.* (1993) results with essentially no errors. Velocity profiles for other Reynolds numbers were also benchmarked with excellent agreement.

To demonstrate the effect of different heat flux input conditions, Figure 5 shows the axial velocity profiles for a triangular heat flux input in the evaporator section instead of the uniform heat flux input as shown in Figure 4. All other conditions and geometric dimensions are the same as in Figure 4. It can be seen from Figure 5a that the axial velocities at the evaporator are very different than the case for uniform heat flux inputs as shown in Figure 4. There is no surprise that the maximum axial velocity is larger for the case of triangular heat flux input since more heat enters the first half of the evaporator section. This causes more vapors to be generated, thus leading to higher maximum axial velocity. Note that

the blowing velocity is directly proportional to the heat flux input (see equation (7)). When the heat pipe is stationary (i.e., 0 rpm), the axial velocity profile is parabolic. As the rotating speed increases, a significant change is seen in Figures 4 and 5. Near the heat pipe wall, the vapor axial velocity increases as the rotating speed increases. This is because the Coriolis and centrifugal force are both acting in the radial direction (see Table 1). The Coriolis force, $2\rho\Omega V_\theta$ depends on two components, V_θ and Ω. Larger rotating speed Ω and/or larger circumferential velocity V_θ, causes larger axial velocity gradient near the wall because these forces are squeezing the flow from the center to the wall. It is worth pointing out that the other Coriolis force term, $2\rho\Omega V_r$ (see Table 1), also plays a significant role in determining the circumferential velocity, V_θ, which in turn affects the Coriolis force in the radial direction. Due to the stronger heat flux input in the first half of the evaporator section, the radial velocity (i.e., blowing velocity) is larger, thus increasing the strength of the circumferential velocity, and the Coriolis force in the radial direction. This larger axial velocity gradient can be seen in Figure 4a. As the rotating speed increases further, it can be seen that the axial velocity gradient increases significantly. However, in the core region, the axial velocity decreased significantly with increasing rotating speed. This is because the increase in mass flow rate near the wall region must be balanced by the decrease in the mass flow rate near the core region to conserve mass. As the rotating
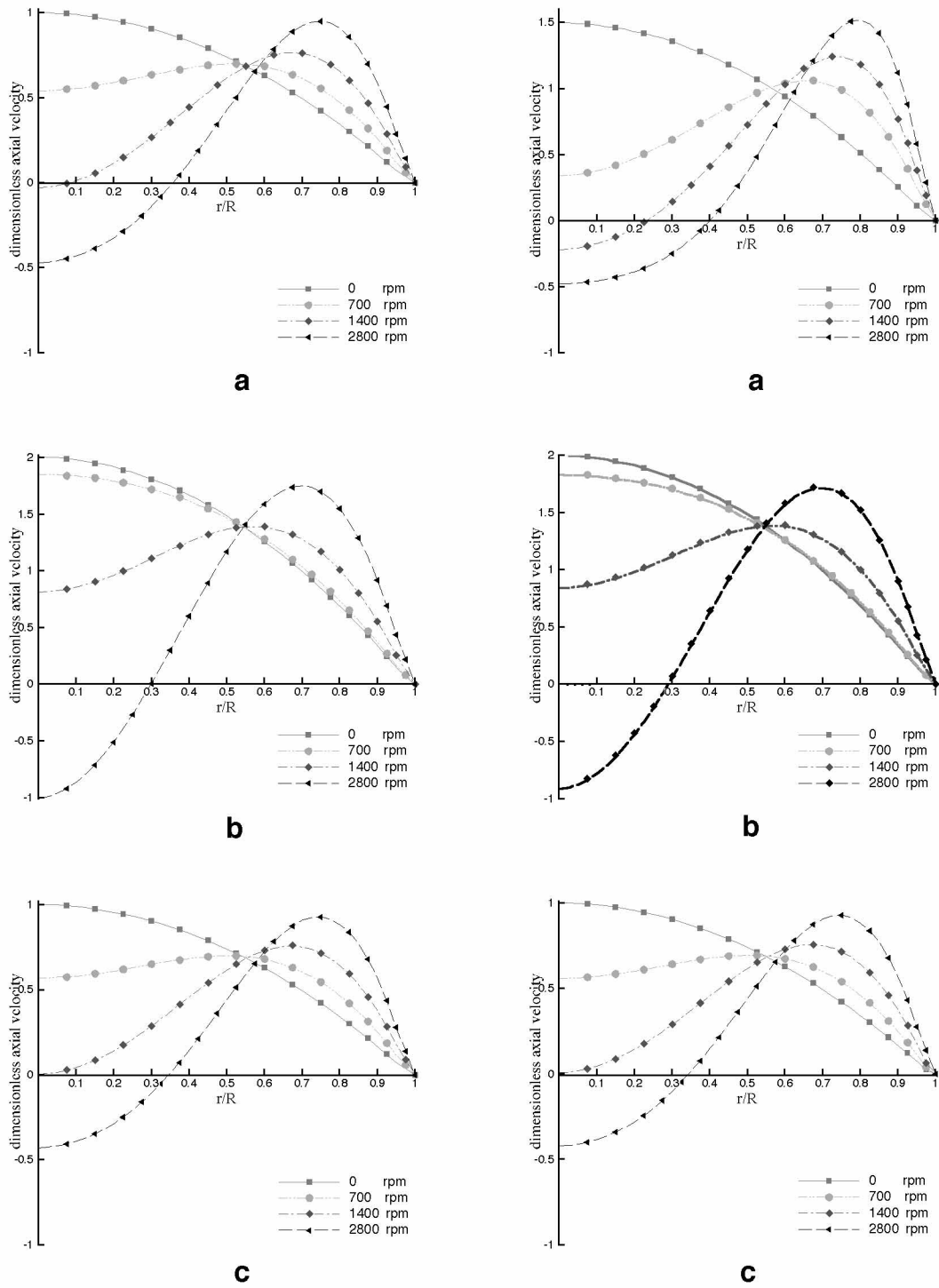
FIGURE 3
Physical domain and coordinate.

TABLE 3
Heat Pipe Geometry and Parameters.

Le	0.025 m	Q_{total}	*85 W*
La	0.15 m	μ	10^{-5} kg/(m s)
Lc	0.025 m	h_{fg}	2300 KJ/kg
D	0.015	R_v	0.4615 KJ/(kg K)

TABLE 4
Saturation Conditions and Blowing Velocities.

$Psat$ (Pa)	$Tsat$ (...C)	ρ (kg/m^3)	V_w (m/s)	Re
15000	53.4	0.1	0.3151	
40000	75.8	0.248	0.1263	
				23.6
70000	90	0.418	0.0751	
101000	100	0.586	0.0535	

speed increases to 1200 rpm, core region flow reversal is observed. Figures 5b and c demonstrate the effect of different rotating speeds on the axial velocity distributions at adiabatic section and at the condenser section, respectively. It is noted that, in comparison to Figures 4b and c, the velocity profiles at the center of the adiabatic region and of the condenser are almost the same. This indicates that the changes in the input condition (i.e., from uniform to triangular heat flux distribution) at the evaporator do not have a strong effect of the velocity distribution at the adiabatic and the condenser sections. It can be seen that the axial vapor flow has achieved a fully developed condition in the adiabatic region. The movement of the region of maximum velocity to the heat pipe wall with increasing rotational speed is referred to as the Ekmann suction in rotating flow (Hocking, 1967). It is important to note that even for small Reynolds number, such as $Re=0.01$, separation can occur for increasing rotating speed. This turns the problem into a fully elliptic one. In the case of a triangular heat flux distribution, separation at the evaporator occurs for lower rotating speed as it can be seen from comparison between Figure 4a and Figure 5a. In the present study, we are aiming at a fundamental study of vapor flow on an application of heat pipe drill for drilling operation conditions. The dimension of the heat pipe and parameters for the current study are summarized in Table 3:

This type of heat pipe, which has been inserted ion the drill, is significantly different from the one used in Faghri, *et al.* (1993). The heat pipe used in this study has much shorter evaporator section and condenser section. This is because the heat is concentrated only in the drill tip area, thus a smaller heat input area are required. Note that this may cause higher heat flux
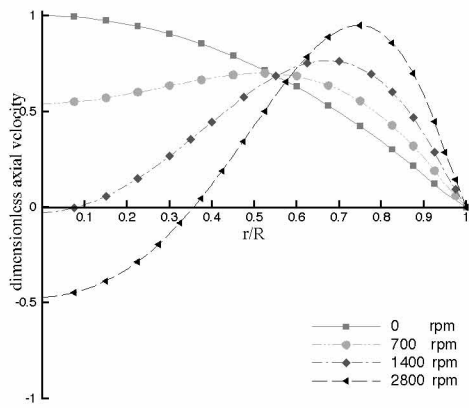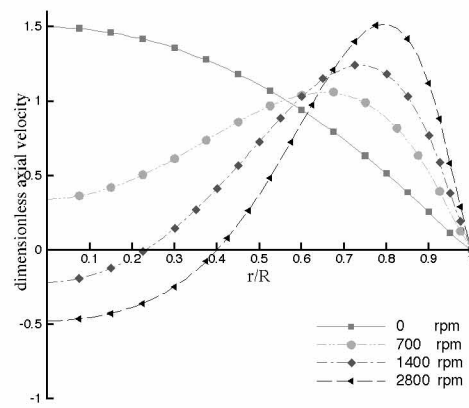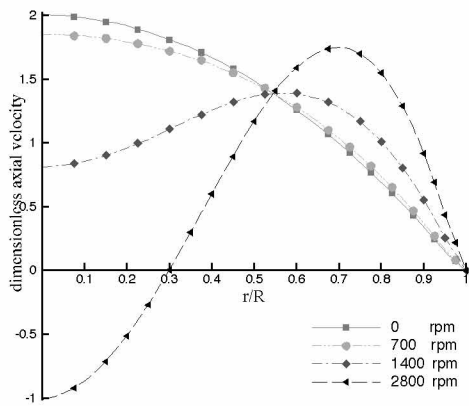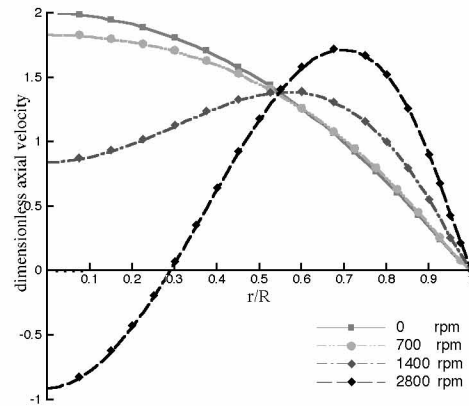
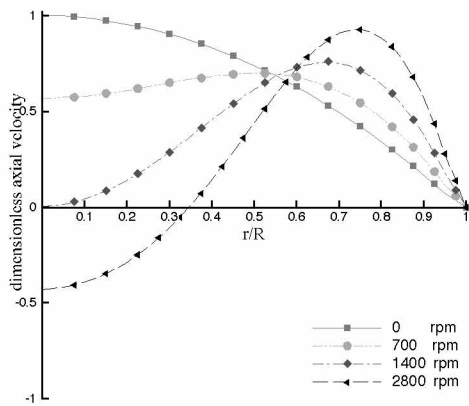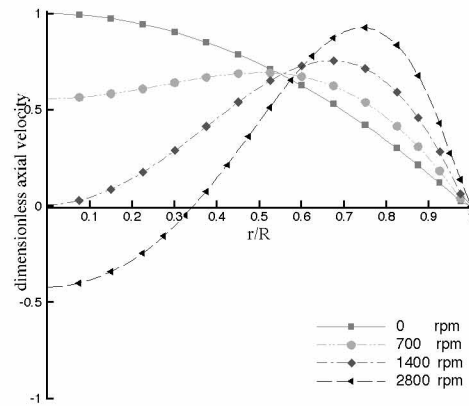FIGURE 4
Axial velocity profiles (for a uniform heat flux, Faghri *et. al.* (1993)) at the middle of a) Evaporator, b) Adiabatic region, c) Condenser.

FIGURE 5
Axial velocity profiles (for a triangular heat flux distribution) at the middle of a) Evaporator, b) Adiabatic region, c) Condenser.

input due the large intensity of the heat generation in the drill tip area. The density is calculated from the equation of state (9) for different saturation conditions. Four different saturation conditions were studied (Note that the working condition depends on saturated temperature or working temperature):

For each of these cases, four different rotational speeds were assumed: 0, 400, 800 and 1200 rpm (0, 41.89, 83.78 and 125.66 rad/s). The heat flux distributions at the evaporator and the condenser were calculated from the condition that the amount of heat entering and leaving the pipe has to be the same.

Figures 6, 7, 8 and 9 show dimensionless axial velocity profiles for four different saturation temperatures: 100 ºC, 90 ºC, 75.8 ºC and 53.4 ºC respectively, as a function of the dimensionless radial coordinate r/R. In these figures, dimensionless axial velocities are normalized with the suction velocity, V_w, at the condenser region. In all the cases the heat flux input and the Reynolds number are kept the same.

In the work by Faghri *et al.* (1993), a fixed saturation temperature (i.e., 100ºC) was assumed in their study, while the Reynolds number and the rotating speed are varied. However, it is worth pointing out that for different saturation temperatures, the density, the blowing velocity as well as the hydrodynamics of the flow change. It is not enough to specify only the Reynolds number and the rotational speed to completely define the problem. It will be demonstrated that the saturation temperature plays an important role in the vapor flow velocity distribution. If we compare the results depicted in Figures 6, 7, 8, and 9, it can be seen clearly that the saturation temperature has a strong effect on the axial velocity distribution.

It can be seen from these four figures (Figures 6, 7, 8, and 9) that when the saturation temperature decreases, the effect of the Coriolis force diminishes. This is because the lower the saturation temperature results in smaller vapor density (see Table 4). Note that the Coriolis forces depend on the magnitude of the density (see Table 1). When the saturation temperature decreases from 100ºC to 53.4ºC, the density changes by a factor of approximately 6 (i.e.,

from 0.586 kg/m³ to 0.1 kg/m³), implying a reduction in Coriolis force by the same factor. By decreasing the saturation temperature, the velocity profiles approaches to the cases without rotation as shown in Figure 9. Note that in the typical stationary blowing/suction heat pipe condition, the blowing boundary condition tends to stabilize the flow, and the suction boundary condition tends to destabilize the flow, and thus the flow reversal can be seen in the condenser section. It is also interesting to note that the rotating effect in the condenser section tends to stabilize the flow due to the circumferential Coriolis force.

Figures 10 and 11 show the dimensionless radial velocity profiles normalized with the suction velocity at the condenser V_w as a function of the radial coordinate r/R, for the case with saturation temperature at 100ºC and 53.4ºC, respectively. Note that at the evaporator, the input velocity at the wall (r/R=1.0) is negative (blowing) and positive (suction) at the condenser. For T_{sat}=100 ºC in Figure 10a, a negative radial velocity at the evaporator for rotating speed up to 400 rpm was observed. It can be seen that at 400 rpm, the radial velocity near the center becomes very small. With further increase in rotational velocity, the slope of the radial velocity becomes nearly zero. This implies that the axial velocity is negative, a sign of flow reversal. The reason that this happens is because the rotating effect causes the axial velocity gradient to increase, and thus in order to satisfy mass conservation, axial flow reversal occurs near the core region of the heat pipe. Therefore, the radial velocity becomes positive to satisfy continuity. Similar reason can be applied to the condenser section (Figure 10c), where the wall boundary condition now changes to suction condition (i.e., positive radial velocity). Thus, a negative axial velocity implies the radial flow becomes negative (i.e., flow reversal). For the case with T_{sat} = 53.4ºC, the rotating induced Coriolis forces have diminished greatly as explained above, thus the variation of radial velocity due to Coriolis force effect is also insignificant as shown in Figure 11.

Figures 12 and 13 show circumferential velocity profiles as a function of the radial coordinate r/R for the cases with T_{sat} = 100 ºC and T_{sat} = 53.4 ºC,
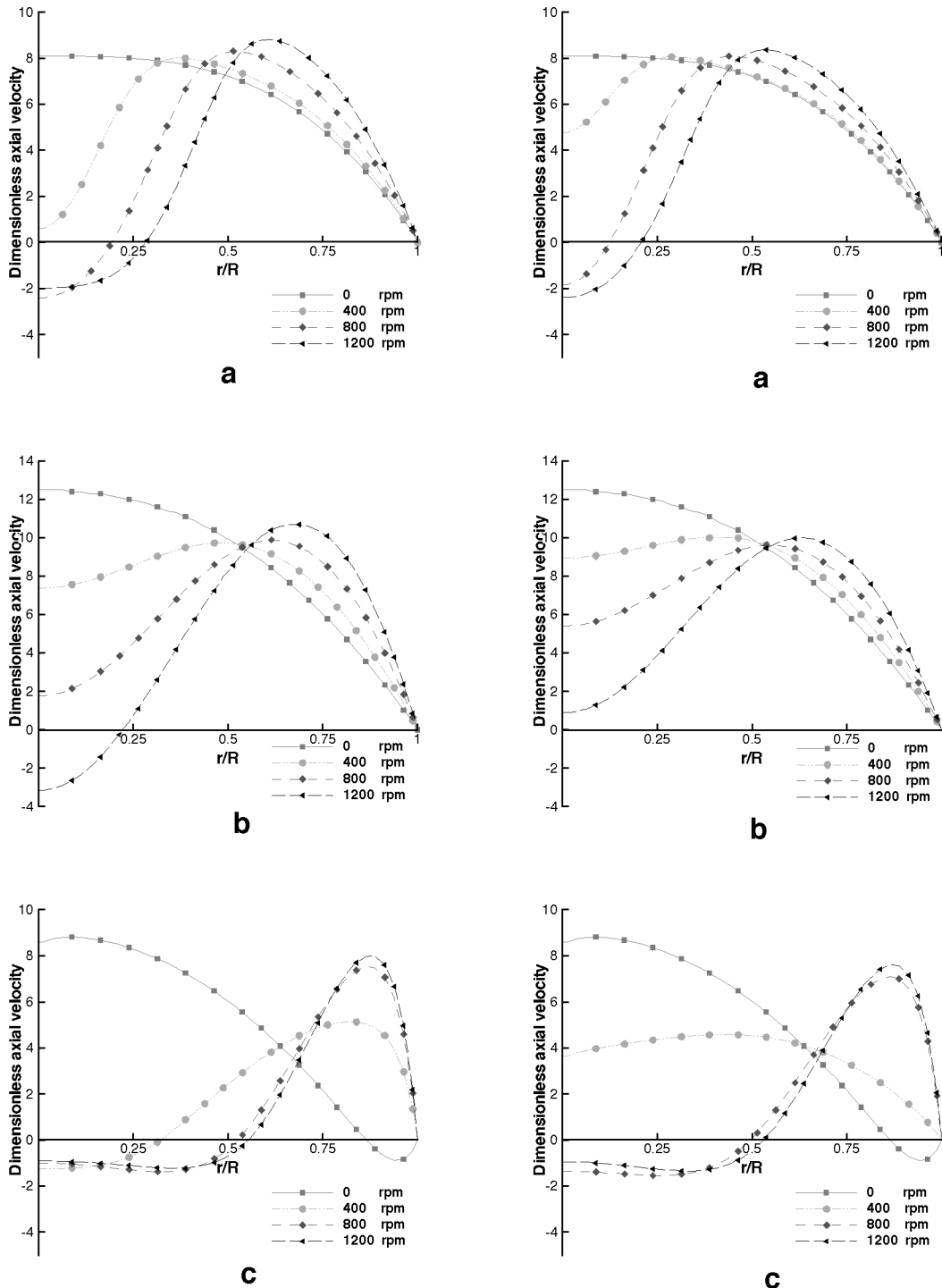
FIGURE 6
Axial velocity profiles (for a triangular heat flux distribution) at the middle of a) Evaporator, b) Adiabatic region, c) Condenser. T_{sat} = 100 ºC.

FIGURE 7
Axial velocity profiles (for a triangular heat flux distribution) at the middle of a) Evaporator, b) Adiabatic region, c) Condenser. T_{sat} = 90 ºC.
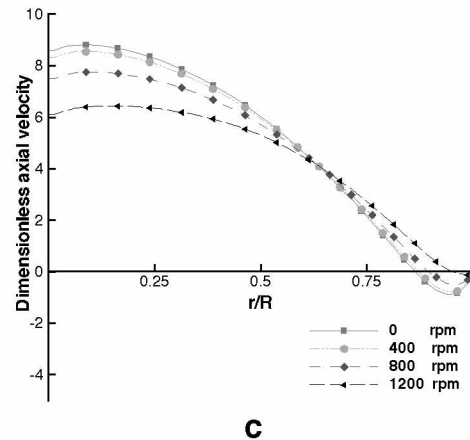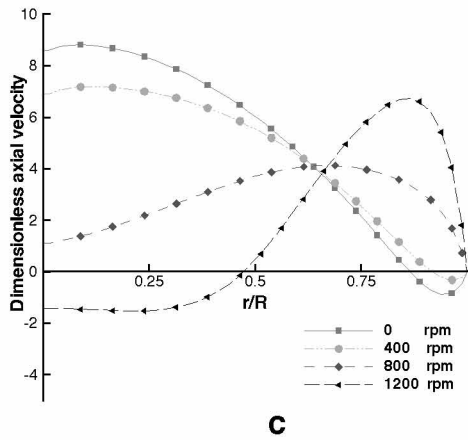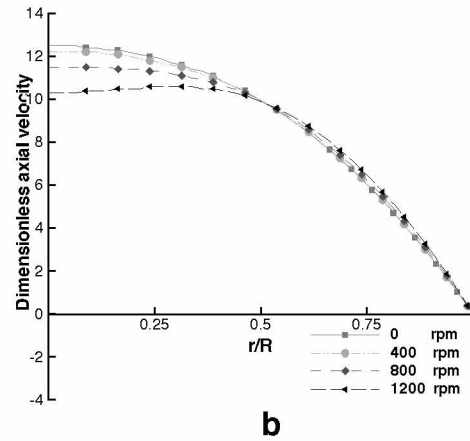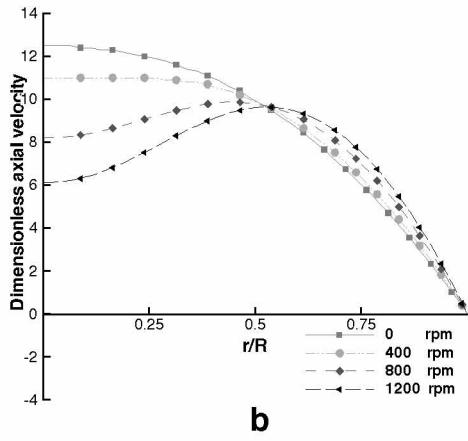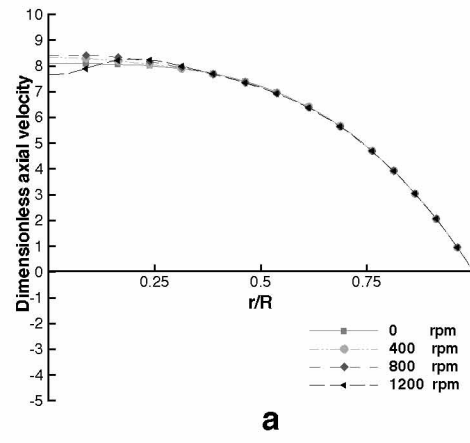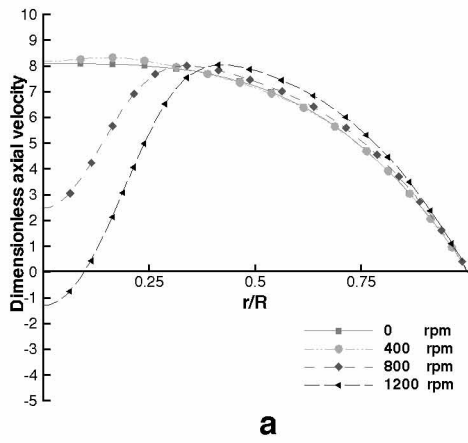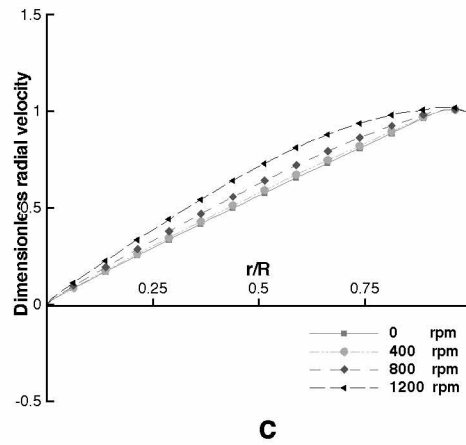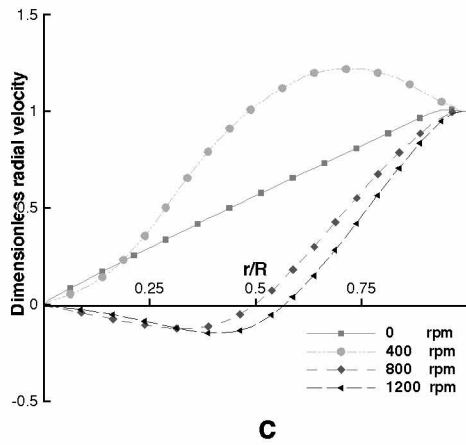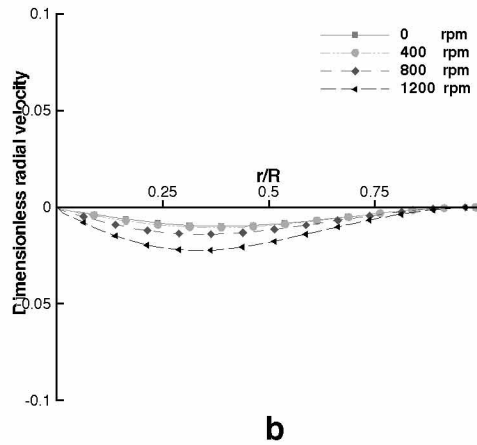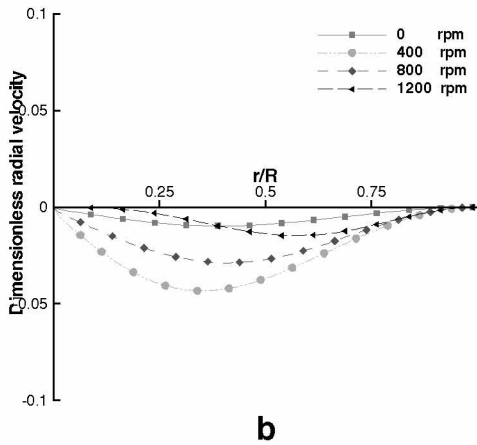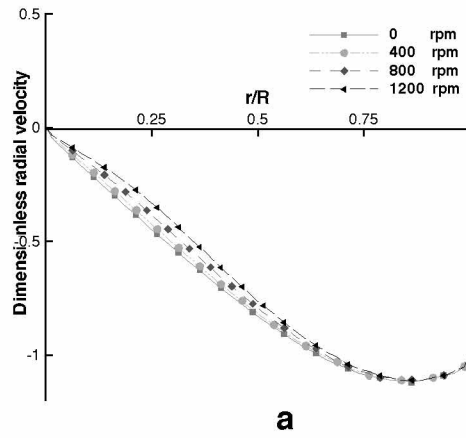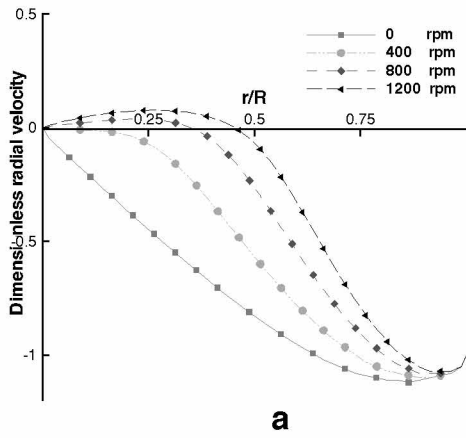
FIGURE 8
Axial velocity profiles (for a triangular heat flux distribution) at the middle of a) Evaporator, b) Adiabatic region, c) Condenser. $T_{sat} = 75.8$ ºC.

FIGURE 9
Axial velocity profiles (for a triangular heat flux distribution) at the middle of a) Evaporator, b) Adiabatic region, c) Condenser. $T_{sat} = 53.4$ ºC.

FIGURE 10
Radial velocity profiles (for a triangular heat flux distribution) at the middle of a) Evaporator, b) Adiabatic region, c) Condenser. T_{sat} = 100 ºC.

FIGURE 11
Radial velocity profiles (for a triangular heat flux distribution) at the middle of a) Evaporator, b) Adiabatic region, c) Condenser. T_{sat} = 53.4 º.

FIGURE 12
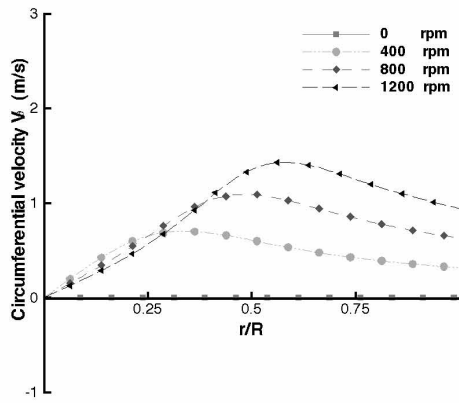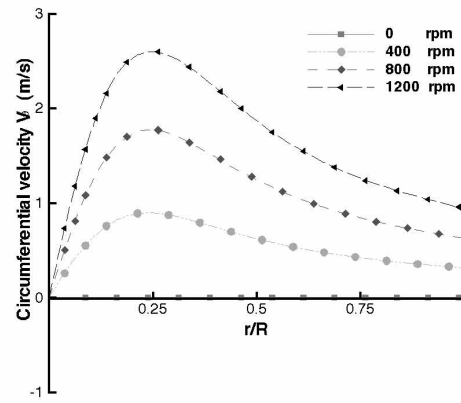Circumferential velocity profiles (for a triangular heat flux distribution) at the middle of a) Evaporator, b) Adiabatic region, c) Condenser. $T_{sat} = 100$ ºC.

FIGURE 13
Circumferential velocity profiles (for a triangular heat flux distribution) at the middle of a) Evaporator, b) Adiabatic region, c) Condenser. $T_{sat} = 53.4$ ºC.
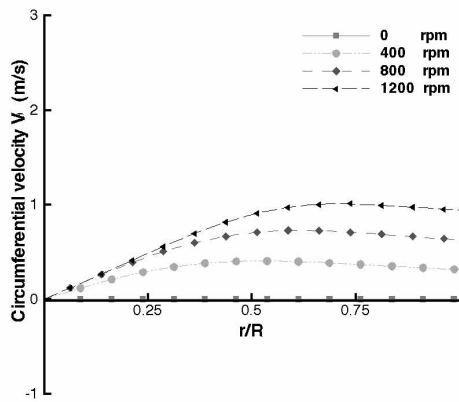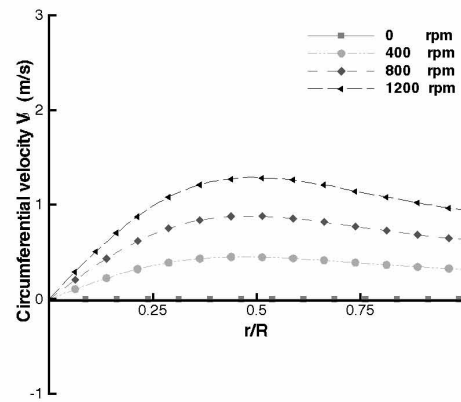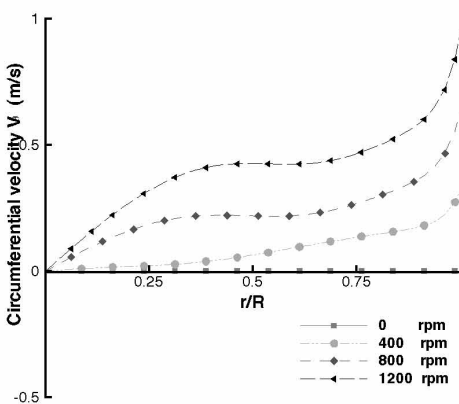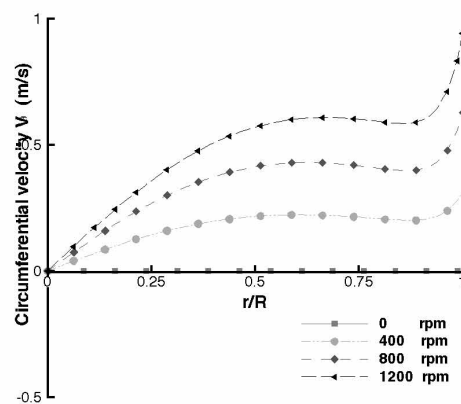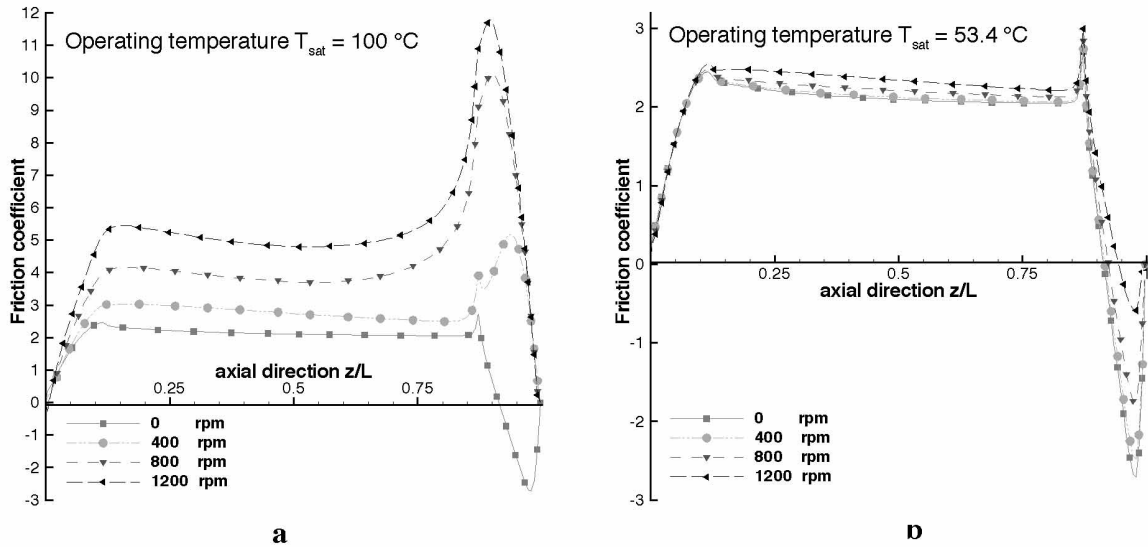
FIGURE 14
Friction factor along the pipe for different rotating speeds.

respectively. For solid rotation, the circumferential velocity is a linear function of r, $V_\theta = \Omega\, r$. However, with the effect of Coriolis force, the circumferential velocities are no longer linear as shown in Figures 12 and 13. In the evaporator section, Figures 12a and 13a, it can be seen that the circumferential velocity increases significantly due to the Coriolis force, $2\rho\Omega V_r$, which is aiding the flow in the same direction of the solid rotation. Due to the no-slip boundary condition, the circumferential velocity at the wall equals the solid rotation velocity. The circumferential velocities are larger for the case of low saturation temperature (i.e., T_{sat} = 53.4 °C) because the radial velocity is larger as shown in Figure 11a. In the adiabatic section, since the radial velocities are small, the distortions of the velocity profiles due to the Coriolis forces are not significant. In the evaporator section, however, the trends are reverse. In Figures 12c and 13c, the circumferential velocities near the heat pipe wall have been suppressed significantly. This effect is stronger for the case with higher saturation temperature case, T_{sat} = 100 °C, since the Coriolis force is stronger in the θ direction at this temperature.

Figure 14 shows the development of the friction coefficient along the pipe in the r-z plane. For all the cases presented in this study the Reynolds number is the same, so the friction coefficient f is a measure of the axial velocity gradient at the wall (see equation (11)). It can be seen that the friction coefficient increases monotonically in the evaporator region due to the development of the axial velocity profiles. At the middle of the adiabatic section the friction coefficient is essentially constant showing that the flow has reached a fully developed condition. Figure 14a also shows that the friction factor increases as the rotating speed is increased. However, the rotating effect on friction coefficient is negligible due to the diminishing effect of Coriolis forces due to low saturation temperature as shown in Figure 14b. It is worth noting that in Figure 14a, the friction coefficient becomes negative for the stationary case (i.e., 0 rpm), this indicates that flow reversal occurs at the condenser section. This is because the suction boundary condition at the condenser section causes the flow reversal. For increasing rotating speeds, the friction coefficient starts to increase and becomes positive at the condenser section. This reveals that the
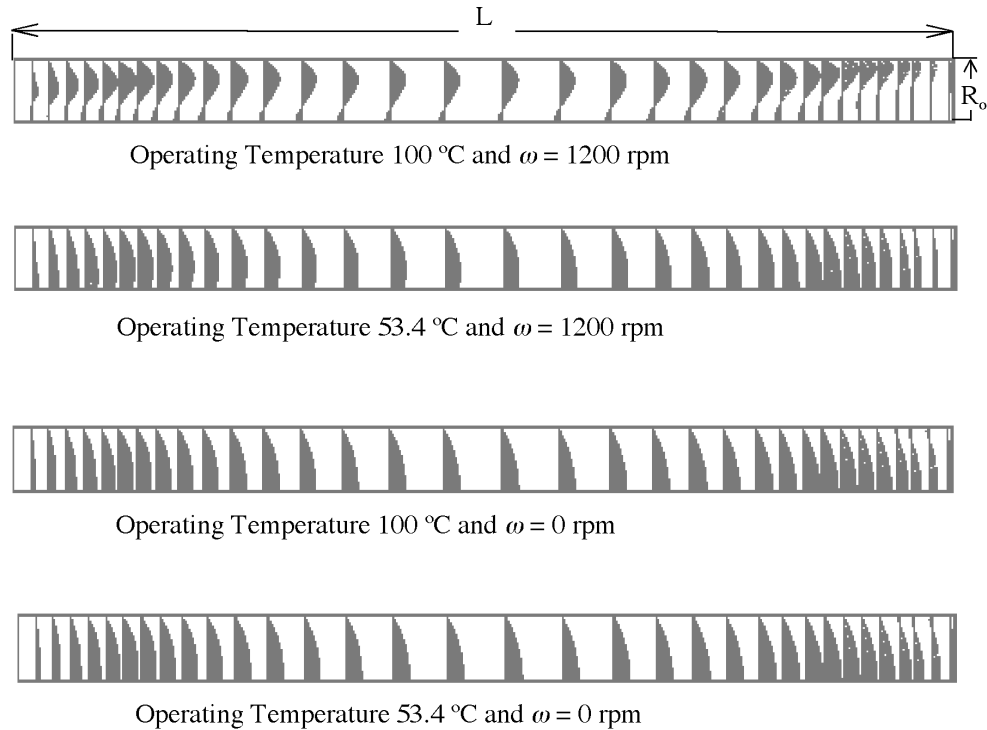
Operating Temperature 100 ºC and $\omega = 1200$ rpm

Operating Temperature 53.4 ºC and $\omega = 1200$ rpm

Operating Temperature 100 ºC and $\omega = 0$ rpm

Operating Temperature 53.4 ºC and $\omega = 0$ rpm

FIGURE 15
Vector plot in the z-r plane.

Coriolis forces tend to stabilize the flow as described earlier. For lower saturation temperature as shown in Figure 14b, however, throughout the rotating speed range studied (i.e., 0-1200 rpm), the flow reversal exists. Again, this is due to the diminishing Coriolis force effect. It can be seen that the effect of the suction velocity in the condenser propagates farther upstream for increasing rotating speeds at larger saturation temperature as in Figure 14a. In Figure 14b, however, the effect of the suction boundary condition in the condenser is not felt upstream, except in a very short distance. It is important to point out that the magnitude of the velocity gradient in the condenser, for an operating temperature of 100 ºC, is about four times higher than the one for $T_{sat} = 53.4$ ºC for the case of 1200 rpm. This demonstrates the strong local effect of the Coriolis force.

Figure 15 shows a vector plot in the plane *r-z* for a rotating speed of 1200 rpm and 0 rpm at operating temperatures of 100 ºC and 53.4 ºC. It can be seen clearly that for $T_{sat} = 53.4$ ºC the velocity field is not very much influenced by the rotating speed and in the adiabatic section is almost a parabolic profile. Also, the reversal flow at the center of the pipe is clearly seen for the case of $T_{sat} = 100$ ºC and $\omega = 1200$ rpm. This is consistent with results shown in Figures 6 and 9.

CONCLUSIONS

A numerical study was carried out to analyze the effect of rotating speeds and different saturation conditions on the hydrodynamics of the vapor flow of a rotating heat pipe for drilling applications. The following conclusions can be made:

1. For the same amount of total heat input and geometric configuration, flow pattern is strongly influenced by the saturation temperatures as well as the rotating speed.

2. For increasing rotating speeds the axial velocity increases near the wall due to the strong radial Coriolis force acting toward the wall. Meanwhile, the axial velocity near the centerline decreases due to mass conservation and flow reversal can occur at large rotating speed.

3. The Coriolis force is reduced for smaller saturation temperatures where inertial effects dominate. This indicates that for lower saturation temperatures the rotating effect is less important.

4. Flow reversal can occur even for small Reynolds numbers and the problem become fully elliptic. A fully developed condition is reached at the adiabatic section of the heat pipe. Suction boundary condition in the condenser section influences the upstream velocity distribution further as the saturation temperature and the rotating speed are increased.

5. The circumferential velocity deviates very significantly from solid body rotational velocity Ωr. This effect is stronger for decreasing operating temperatures.

6. For numerical analyses, using the coordinate system fixed to the rotating frame (i.e., non-inertial) is recommended since this system shows better numerical stability, especially for high rotating speeds.

The results of this study will be used for a more complete analysis when the liquid flow and heat conduction on the wall as well as the effect of the contact resistance between the heat pipe and the drilling tool are considered.

NOMENCLATURE

D diameter of the heat pipe [m]
f friction coefficient, $2\tau_w / \rho V_w^2$
h_{fg} latent heat of vaporization [J/kg]
L length of the heat pipe [m]
L_e length of the evaporator [m]
L_a length of the adiabatic region [m]
L_c length of the condenser [m]
p pressure [Pa]
P_{sat} saturation pressure
q local rate of heat transfer per unit length [W/m]
Q_{total} total amount of heat entering and leaving the heat pipe [W]
R_0 radius of the heat pipe [m]
R_v gas constant for the vapor [J/(kg K)]
Re Reynolds numbers, Re $= \rho V_w R / \mu$
r, θ, z radial, circumferential and axial coordinates
S_ϕ source term in the generic property ϕ
T_{sat} saturation temperature [ºC]
V_r, V_θ, V_z : Velocities in the r, θ, and z direction respectively [m/s]
V_w blowing and suction velocity at the condenser and evaporator respectively [m]

Greek

ρ density of the vapor [kg/m³]
ϕ generic property
μ dynamic viscosity of the vapor [kg/(m s)]
Γ diffusivity for the generic property ϕ
Ω angular velocity [rad/s]

REFERENCE

Ballback, L., (1969). "The operation of a rotating wickless heat pipe," M.Sc. Thesis, Monterrey, CA, U.S. Naval Postgraduate School (Ad 701674).

Chan, S.H., Kanai, Z. and Yang W.T, (1971). "Theory of a rotating heat pipe," *Journal of Nuclear Energy*, Vol. 25, pp. 479-487.

Daley, T., (1970). "The experimental design and operation of a rotating wickless heat pipe," M.Sc. Thesis, Monterrey, CA, U.S. Naval Postgraduate School (Ad 709923).

Daniels, T. and Al-Jumaily, F., (1975). "Investigation of the factor affecting the performance of a rotating heat pipe," *Int. J. Heat Mass Transfer, Vol. 18*, pp. 961-973.

DeVries, M.F., and Murray, S.F., (1994). "Tribology at the cutting edge: cutting and grinding fluids," *PD-Vol. 61, ASME Tribology Symposium*, pp. 23-33.

Faghri, A., (1995). *Heat Pipe Science and Technology*, Taylor & Francis, Washington, D.C.

Faghri, A. Gogineni, S. and Thomas, S., (1993). "Vapor flow analysis of an axially rotating heat pipe," *Int. J. Heat Mass Transfer*, *Vol. 36*, pp. 2293-2303.

Gray, V., (1969). "The rotating heat pipe-a wickless, hollow shaft for transferring high heat fluxes," ASME-AIChE Heat Transfer Conference, Minneapolis, Minnesota.

Gutierrez, G. and Jen, T.C., (2002) "Experimental investigation of heat pipe drill performance," to be presented at NSF 2003 Design, Service and Manufacturing Grantees and Research Conference, Tuscaloosa, Alabama, January 6-9, 2003.

Harley, C. and Faghri, A., (1995). "Two-dimensional rotating heat pipe analysis," ASME *J. Heat Transfer*, *Vol. 117*, No. 1, pp. 202-208.

Hocking, L.M., (1967). "Boundary and shear layers in a curved rotating pipe," *J. Math. Phy. Sci.*, *Vol. 1*, Nos. 1-2, pp. 123-136.

Jen, T.C., Gutierrez, G., Eapen S., Barber, G., Zhao, H., Szuba, S., Manjunathaiah, J., and Labataille, J., (2002). "Investigation of heat pipes cooling in drilling applications Part I: Preliminary numerical analysis and verifications," *International Journal of Machine Tool and Manufacture, Vol. 42*, No.5, pp. 643-652.

Kalpakjian, S., (1995). *Manufacturing Engineering and Technology*, Addison-Wesley, New York.

Labattaille, J. and Manjunathaiah, J., (1999). "Evaluation of drilling with heat pipe cooling," Lamb Technicon Report LX-0437.

Lock, G.S.H., (1992). *The Tubular Thermosyphon: Variacion on the Theme*, Oxford Science Publications, Oxford.

Patankar, S.V., (1980). *Numerical Heat Transfer and Fluid Flow*, Hemisphere Publishing Corp., Washington, D.C.

Peterson, G.P. and Wu, D., (1991). "A review of rotating and revolving heat pipes," ASME paper, National Heat Transfer Conference, Minneapolis, MN.

Peterson, G.P., (1994). *An Introduction to Heat Pipes: Modeling, Testing and Applications*, Wiley, New York.

Van Doormal, J.P. and Raithby, G.D., (1967). "Enhancements of the SIMPLE method for predicting incompressible fluid flows," *Numerical Heat Transfer*, *Vol. 7*, pp. 147-163.